Research Article Vol. 42, No. 7 / July 2025 / Journal of the Optical Society of America A 1031

Journal of the Optical Society of America A
OPTICS, IMAGE SCIENCE, AND VISION

High-temperature-resistant strain sensor based on the asymmetric tapered Fabry–Pérot fiber

Xinping Song,[1] Jingwei Lv,[1] Jianxin Wang,[1] Wei Liu,[1] Famei Wang,[2] Weiqiang Wang,[1] Zao Yi,[3] Miao Liu,[4] Qiang Liu,[1] Paul K. Chu,[5] and Chao Liu[1,*]

[1]School of Physics and Electronic Engineering, Northeast Petroleum University, Daqing 163318, China
[2]Shenzhen Key Laboratory of Ultra-Intense Laser and Advanced Material Technology, Center for Intense Laser Application Technology, and College of Engineering Physics, Shenzhen Technology University, Shenzhen 518118, China
[3]Joint Laboratory for Extreme Conditions Matter Properties, Southwest University of Science and Technology, Mianyang 621010, China
[4]Qinhuangdao Campus, Northeast Petroleum University, Qinhuangdao, 066044, China
[5]Department of Physics, Department of Materials Science and Engineering, and Department of Biomedical Engineering, City University of Hong Kong, Tat Chee Avenue, Kowloon, Hong Kong SAR, China
*msm-liu@126.com

Received 13 February 2025; revised 28 April 2025; accepted 18 May 2025; posted 19 May 2025; published 30 June 2025

A high-temperature-resistant strain sensor based on an asymmetric tapered Fabry–Pérot fiber (FPI) structure is designed and validated experimentally. The strain sensor is constructed by fusing two standard single-mode optical fibers to form a microbubble and applying a taper on one side of the microbubble to form the asymmetric tapered structure. The strain characteristics of the sensor in the temperature range from room temperature to 425°C are determined. A good linear relationship is observed between the wavelength displacement and tensile strain in this temperature range. The strain sensitivity is 47.69 pm/με at 25°C, and the linear response is reproducible in the range of 0–300 με. In addition, the wavelength displacement due to the applied strain is stable with respect to each 100°C increase in the temperature, indicating that the FPI sensor has good temperature stability in the strain range between 0 and 300 με. The average temperature sensitivity is 1.56 pm/°C in the temperature range between 25°C and 425°C, and the cross-sensitivity is very low. Our results show that the FPI sensor has strong resistance to high temperatures, boding well for applications such as aerospace components, metal processing, and gas boilers. © 2025 Optica Publishing Group. All rights, including for text and data mining (TDM), Artificial Intelligence (AI) training, and similar technologies, are reserved.

https://doi.org/10.1364/JOSAA.559487

1. INTRODUCTION

Strain, which describes the deformation degree of materials under an external field, is an important parameter for industrial assessment, medical treatment, and environmental monitoring [1–4]. Compared with traditional resistive strain measurement methods, strain sensors based on optical fibers have the advantages of a compact structure, small size, high sensitivity, corrosion resistance, and resistance to electromagnetic interference [5,6]. They can also be used to measure multiple physical entities such as temperature, pressure, refractive index, magnetic field, and humidity [7–11]. Because industrial components, such as turbines, furnaces, and control systems, are frequently operated at high temperatures [8], high-temperature strain sensors composed of optical fibers have attracted much attention [12–16].

Changes in the thermo-optic coefficient and thermal expansion coefficient of an optical fiber with temperature lead to changes in the refractive index and physical dimensions of the fiber, consequently producing spectral shifts and high strain–temperature cross-sensitivity [17,18]. In order to reduce the effects of strain and temperature, various temperature compensation methods have been used, for instance as introducing a reference fiber that is independent of temperature variations [19], integrating temperature-sensing elements [20], and algorithmic processing of signal decoupling using complex mathematical models [21]. However, these can result in higher strain measurement costs and high manufacturing complexity.

The cavity in the Fabry–Pérot interferometer (FPI) has the unique advantage of mitigating strain–temperature cross-sensitivity [22–26]. Since the coefficient of thermal expansion of air is much smaller than that of optical fiber materials, the air cavity size and its effect on spectral shifts are smaller with changing ambient temperature, consequently reducing the thermal sensitivity and strain–temperature cross-sensitivity [27,28]. Several methods have been reported for fabricating FP strain sensors. For example, Tian *et al*. have used femtosecond laser micromachining and optical fiber fusion to embed two tapered single-mode optical fibers into a hollow-core optical fiber to

form the SMF–HCF–SMF structure with a strain sensitivity of 142.2 pm/με, low-temperature sensitivity of 2.19 pm/°C in the range of 0–200°C, as well as low temperature–strain cross talk below 16.6 nε/°C [29]. Su *et al*. have fabricated an all-fiber Fabry–Pérot microcavity interferometer based on a t-structure by vertically fitting a single-mode optical fiber onto the symmetric surface of a polished hollow fiber using the side-focusing method and laser polishing. The strain sensitivity is 4.502 pm/με in the range of 0–1200 pm/με, and it is insensitive to temperature changes in the range of 20–80°C [30]. However, the fabrication process of these sensors is relatively complex and expensive, and there are still some limitations concerning their stability and sensitivity in high-temperature environments. Furthermore, the cross-sensitivity issue under high-temperature conditions must still be addressed because in a complex environment, the temperature change may cause an unwanted strain response, which undermines the accuracy of the strain measurement [31–33].

Herein, a high-temperature strain sensor based on the asymmetric tapered FPI principle is designed and demonstrated. A fusion splicer was used to fuse the two single-mode optical fibers to form a tiny microcavity. The microbubbles repeatedly deviate from the center of the discharge to form an asymmetric tapered structure. This design reduces the silica thickness around the bubbles to only 1.89 μm, thus changing the refractive index distribution of the optical fiber microcavity, enhancing the optical interference effect, and improving the strain sensitivity of the sensor, especially in high-temperature environments. Compared to the conventional symmetric FPI structure, this asymmetric design improves the response of the sensor to strain and temperature changes. The strain sensitivity of the asymmetric tapered FPI is 47.69 pm/με at a resonant wavelength of 1550 nm, and the temperature sensitivity is 1.56 pm/°C for a temperature range of 25–425°C, indicating that the sensor is suitable for high-temperature conditions. Owing to its temperature resistance, high strain sensitivity at high temperatures, good repeatability, and low cost, it has great potential in many demanding engineering applications such as aerospace components, metal processing, and boilers.

2. SENSOR PREPARATION, PRINCIPLES, AND THEORETICAL ASSESSMENT

This sensor is composed of an asymmetric conical cavity with a microbubble structure, aiming to reduce the silica content in the Fabry–Pérot cavity and enhance the strain sensitivity. The manufacturing process is illustrated in Fig. 1. As shown in Fig. 1(a), first, pliers are used to remove the coating from the single-mode optical fiber and wipe it clean with alcohol cotton. Subsequently, a cutter was used to smooth the end face of the optical fiber. By controlling the left and right stepper motors, the optical fiber was placed at an appropriate position in the optical fiber fusion splicer (Fujikura 80s). With a discharge power of "−5" and a discharge time of 800 ms, the end face of the optical fiber is heat-melted into an arc shape, as shown in Fig. 1(b). Subsequently, as shown in Fig. 1(c), the end faces of the two single-mode optical fibers were immersed in a small amount of refractive index-matching fluid (Nd: 1.47) and placed back into the optical fiber splicer. The refractive index-matching fluid is an oily substance with good stability, fluidity, and low surface tension, which can effectively fill the gap between the optical fibers, thereby enhancing adhesion and improving light transmission efficiency. As shown in Fig. 1(d), the two single-mode optical fibers were aligned using the three-dimensional adjustment function of the splicer and were slightly squeezed. During this process, the discharge power and discharge time were increased to "+20" and 1200 ms, respectively, for splicing, thus forming a small bubble, as shown in Fig. 1(e). As the left and right motors of the fusion splicer moved to the left, the discharge power and discharge time were simultaneously reduced, and the microbubbles began to move from the center of the discharge area, as shown in Fig. 1(f). After several discharge pulses and applied stress processes, as shown in Fig. 1(g), an asymmetric tapered FP cavity structure was ultimately formed, as illustrated in Fig. 1(h). The tapered region reduces optical energy loss and enhances the contrast of the interference spectrum. The asymmetric design further destroys the symmetry of conventional FP cavities, making the interference spectrum more sensitive to changes in cavity length.

Figure 2 illustrates the optical microscope images, reflectance spectra, and specific parameters of the UATFPI. As can be seen in Fig. 2(a), the length of the cone waist is 48.5 μm, the transverse length of the cavity is 54.77 μm, and the longitudinal length is 60.05 μm. After repeated adjustments, the thickness of the upper wall was reduced to approximately 1.89 μm, and the thickness of the lower walls was reduced to approximately 2.33 μm. The results of reflectance spectroscopy measurements are shown in Fig. 2(b). The free spectral range (FSR) is 19.8 nm, and the extinction ratio (ER) is 15.067 dB, which is suitable for industrial strain monitoring and large dynamic range measurement scenarios. It should be noted that the presence of the conical waist may lead to an expansion of the optical field pattern, which slightly increases the effective cavity length and reduces the FSR. However, no significant deviation was observed in this study, suggesting that the structure does not disrupt the resonance conditions.

The sensing principle of the UATFPI is illustrated in Fig. 3, in which M_1 and M_2 are the two end surfaces of the air microcavity, and the UATFPI is formed between M_1 and M_2. When incident light with intensity $\boldsymbol{I_0}$ emitted from the broadband light source impinges on the SMF, reflection occurs when it reaches the reflecting surface M_1. The intensity of the reflected light is $\boldsymbol{I_1}$, and a portion of the light passes through the reflecting surface M_1 and is transmitted forward through the air cavity to the reflecting surface M_2, where it is reflected again. The intensity of the second reflected light is $\boldsymbol{I_2}$. These two reflected beams are coupled within the core of the SMF to produce interference. Since the reflectivity of quartz is only 4%, only the interference between the two surfaces is considered here. The interference between the two beams is expressed as

$$I = I_1 + I_2 + 2\sqrt{I_1 I_2}\cos(\theta), \tag{1}$$

where $\boldsymbol{I_1}$ and $\boldsymbol{I_2}$ are the light intensities of the two reflected beams, and θ is the phase of the light wave. Interference fringes are produced when $\theta = (2m+1)\pi$, where m is the number of fiber interference levels. λ_{m+1} and λ_m represent the wavelengths of the adjacent interfering troughs, and the FSR can be expressed as

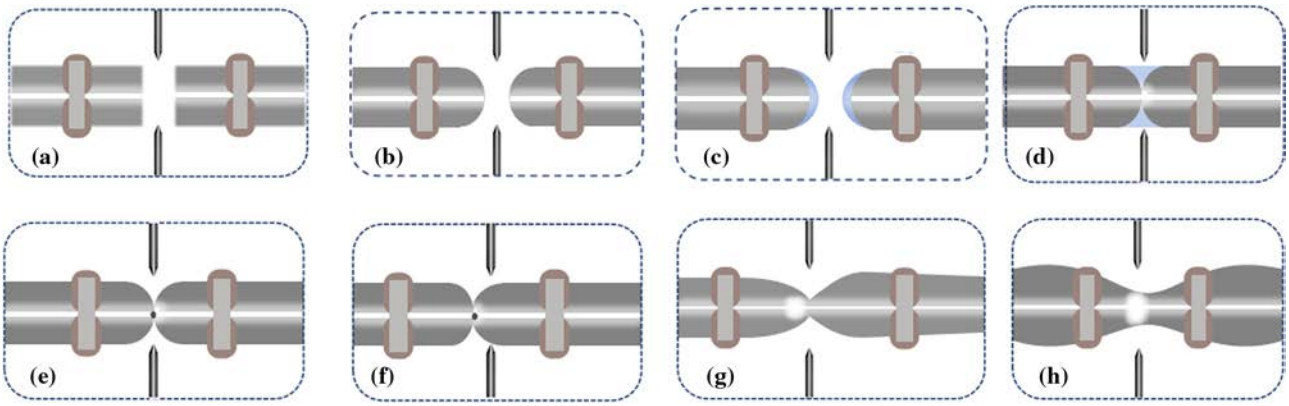

Fig. 1. Schematic illustration of the fabrication of the UATFPI.

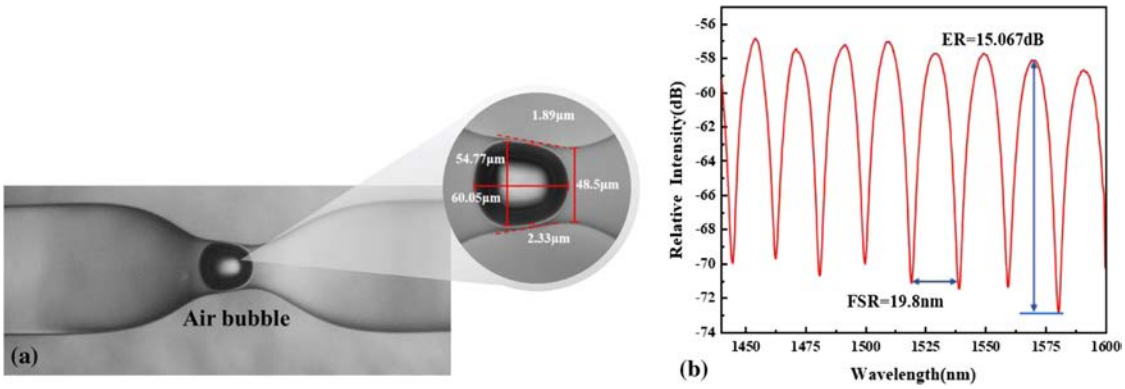

Fig. 2. (a) Microscopic image of the in-fiber FPI with a cavity length of 30 μm in an asymmetrical tapered fiber and (b) reflection spectra.

$$\mathrm{FSR} = \lambda_{m+1} - \lambda_m, \tag{2}$$

$$\mathrm{FSR} = \frac{\lambda_{m+1}\lambda_m}{2nL_{\mathrm{bubble}}}, \tag{3}$$

where n is the refractive index of the air in the air-microbubble, and L_{bubble} is the cavity length of the UATFPI. The refractive index n does not change because the sensor has a closed silica wall, and the medium in the bubble is not exchanged with the outside. The shape of the cavity changes due to stress. The cavity length L changes, causing the wavelength of the trough to shift to a longer wavelength and producing a red shift. The wavelength shift of the interference fringes can be expressed by

$$\Delta\lambda_{\mathrm{bubble}} = k\varepsilon_{\mathrm{bubble}}, \tag{4}$$

where k and $\varepsilon_{\mathrm{bubble}}$ are the strain sensitivity and applied strain of the microbubble structure, respectively. According to the theoretical analysis, the strain coefficient of the structure near the interference peak of 1550 nm is 1.55. Since the cavity length is negligible with respect to the length of the optical fiber, the strain loading relation applied to the microcavity and the SMF is given as follows:

$$\varepsilon_{\mathrm{bubble}} E S_{\mathrm{bubble}} = \varepsilon_{\mathrm{SMF}} E S_{\mathrm{SMF}}, \tag{5}$$

where E is the Young's modulus of the material, and S_{bubble} and S_{SMF} are the cross-sectional areas of the microcavity and SMF, respectively. The axial strain acting on the microcavity and SMF can be expressed as follows [28]:

$$\varepsilon_{\mathrm{SMF}} = \frac{\Delta L_{\mathrm{SMF}}}{L_{\mathrm{SMF}}}, \quad \varepsilon_{\mathrm{bubble}} = \frac{\Delta L_{\mathrm{bubble}}}{L_{\mathrm{bubble}}}, \tag{6}$$

where L_{bubble} and L_{SMF} are the lengths of the microcavity and single-mode fiber, respectively. The total strain magnitude is

$$\varepsilon_0 = \frac{\Delta L_{\mathrm{SMF}} + \Delta L_{\mathrm{bubble}}}{L_{\mathrm{SMF}} + L_{\mathrm{bubble}}}. \tag{7}$$

The above equation, after some algebraic manipulation, is converted into a specific expression for the wavelength displacement as shown:

$$\Delta\lambda_{\mathrm{bubble}} = k\frac{L_{\mathrm{bubble}} + L_{\mathrm{SMF}}}{L_{\mathrm{bubble}}\frac{d_{\mathrm{SMF}}^2 - d_{\mathrm{bubble}}^2}{d_{\mathrm{SMF}}^2} + L_{\mathrm{SMF}}}\varepsilon_0, \tag{8}$$

where d_{bubble} and d_{SMF} are the diameters of the microcavity and single-mode fiber, respectively. By combining the relationship between the wavelength drift and strain of the fiber FPI interference spectrum, the strain sensitivity of the FP cavity fiber strain sensor can be obtained:

$$S = \frac{\Delta\lambda}{\varepsilon_0} = k\frac{L_{\mathrm{bubble}} + L_{\mathrm{SMF}}}{L_{\mathrm{bubble}}\frac{d_{\mathrm{SMF}}^2 - d_{\mathrm{bubble}}^2}{d_{\mathrm{SMF}}^2} + L_{\mathrm{SMF}}}. \tag{9}$$

According to the interference theory of light, the wavelength corresponding to a wave peak in the FPI reflectance spectrogram can be expressed as

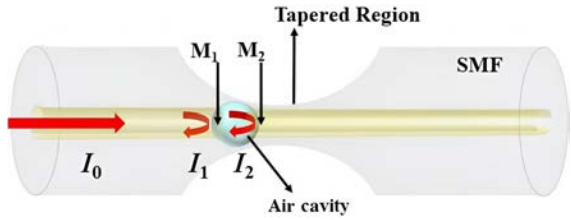

Fig. 3. Schematic diagram of an asymmetric microcavity-based in-fiber FPI strain sensor.

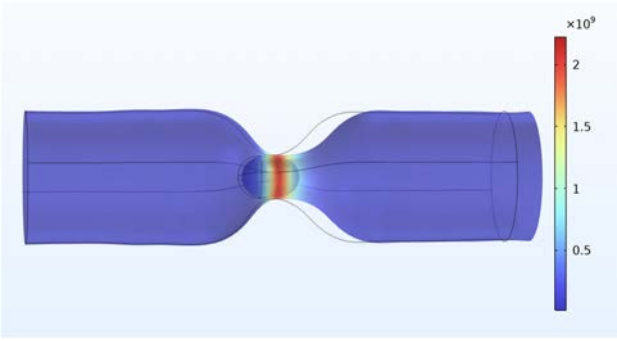

Fig. 4. Deformation of the structure containing asymmetric cones.

$$\lambda = \frac{2n_{\text{eff}}L}{m}. \tag{10}$$

When only the temperature change is considered, the temperature sensitivity ST of the FPI is determined by the following equation:

$$S_T = \frac{\Delta\lambda}{\Delta T} = \left(\frac{1}{L}\frac{\Delta L}{\Delta T} + \frac{1}{n_{\text{eff}}}\frac{\Delta n_{\text{eff}}}{\Delta T}\right)\lambda = (\alpha + \kappa)\,\lambda \tag{11}$$

where T is the temperature, α ($0.55 \times 10^{-6}/°\text{C}$) is the thermal expansion coefficient of silicon, and κ($8.3 \times 10^{-6}/°\text{C}$) is the thermo-optic coefficient of silicon. The variation of the FPI measurement temperature is determined by the thermo-optic effect of the optical fiber, thermal expansion, and the wavelength corresponding to the interference peak. The conical FP cavity structure has relatively less SiO_2. In addition, Eq. (9) shows that shrinking the thickness of the silica wall by shortening the cavity length L_{bubble} or increasing the cross-sectional diameter d_{bubble} can enhance the strain sensitivity of the microbubble structure in the cavity.

The relationship between the cavity length and strain of the FPI under stress is analyzed by finite element analysis. Figure 4 shows the stress distribution of the non-conical structure. The color gradient indicates the stress distribution in different parts of the sensor, where red–yellow and blue–green correspond to the highest and lowest levels of strain, respectively. It can be clearly observed that the strain effect is mainly concentrated on the bubbles. The amount of silica constituting the air cavity decreases with increasing d_{bubble}, and the region with the least amount of silica is subjected to the highest axial stress. Therefore, the strain sensitivity of the FPI with the thin-walled and tapered structure is greater.

3. SENSOR MEASUREMENTS, PROPERTIES, AND DISCUSSION

A. Sensor Measurements

To demonstrate the high-temperature viability of the strain sensor, a heating box with a maximum temperature of 450°C was placed in the center of the 3D moving platform. Figure 5 shows the schematic of the sensor setup at different temperatures. Incident light from the amplified spontaneous emission (ASE, 450–2500 nm) was transmitted to the sensor through a half-two 3 dB fiber-optic coupler and returned to a spectral analyzer (OSA, AQ6370, Advantest) with a resolution of 0.02. It was used to monitor and record the output spectra. The UATFPI was placed on the heated platform under the protection of a corundum tube. Two K-type thermocouples were attached to the outside of the corundum tube and connected to a temperature technical display meter for sensing and measuring the actual temperature of the UATFPI. The corundum tube is externally wrapped with a layer of aluminosilicate ceramic fiber wool to achieve effective thermal insulation and heat preservation [34]. The heat transfer area and corundum tube adopt high-temperature ceramic connecting rubber; the working temperature range is from −200°C to 1200°C, which meets the reliability requirements of the sensor under high-temperature environments. The sensor was fixed on the 3D moving platform, and the temperature of the heating box was gradually increased from 25°C to 425°C and then decreased gradually to 25°C. Because the sensor has limited ability to withstand strain, it will break naturally when tested to a certain range. Therefore, it is important to avoid choosing too small 3D moving platform distance L in the experiment. The distance between the two fixtures of the 3D moving platform was set to be $L_{\text{fiber}} + L_{\text{bubble}} = 40$ cm, shifting the axial stress applied to the sensor each time by 50 με. The heating box was varied in axial strain each time by adjusting the knobs by 100°C each time.

B. Sensor Properties and Discussion

Figure 6 shows the strain characteristics were determined by performing a fast Fourier transform on the synthetic spectra of UATFPI at room temperature. The FSR of 19.8 nm obtained by Eq. (2) was used, and these two wavelengths were close to 1550 nm. The main interference frequency of the UATFPI was around 0.0533. By multiplying the spatial frequency response with the FSR and rounding the result to 1, the spatial frequency response was validated.

The strain response of the UATFPI was determined at room temperature. The microbubbles were deformed under stress, resulting in a wavelength shift in the reflectance spectrum. Fig. 7(a) shows clear red shifting when the axial strain was increased from 0 to 300 με, with a total wavelength drift of about 21 nm. The wavelength shift at the trough of the reflectance spectra was fitted linearly to the stress change, as shown in Fig. 7(b). The strain sensitivity of UAFPI was calculated to be 47.69 pm/με. When the light was not subjected to axial stress, the first data point was offset due to gravity. This offset had an effect on the linearity of the sensor, but the sensor showed an acceptable stress linearity of $R^2 = 0.99934$.

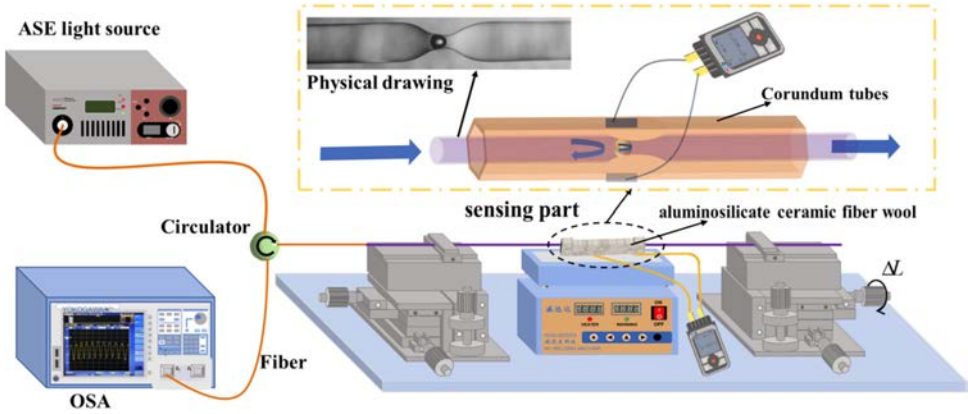

Fig. 5. Optical fiber strain setup.

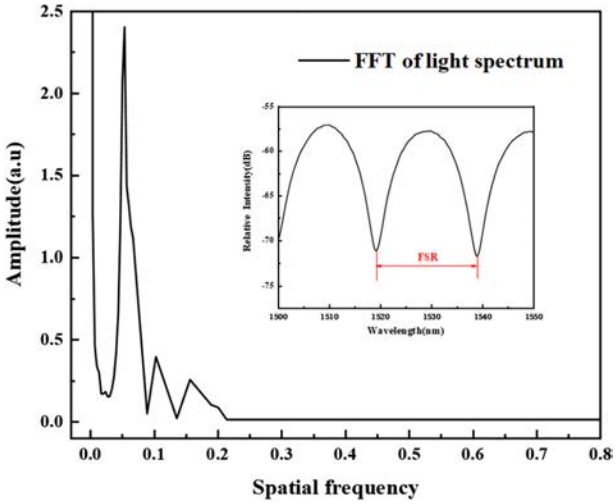

Fig. 6. Spatial frequency spectra of UATFPI.

Repeated experiments were carried out at the ambient temperature of 25°C, and the results are shown in Fig. 8. The linear fitted plots of UATFPI versus wavelength drift under constant applied stress and released stress were obtained to derive the strain sensitivity in both states. The strain sensitivity under stress was 47.69 pm/με with a linearity of 0.99934, and that under released stress was 47.5 pm/με with a linearity of 0.99937. The two lines are almost coincident, verifying that the UATFPI has good reproducibility and stability.

Due to the influence of the material itself, optical fiber sensors sensitive to other physical fields may encounter temperature–strain crosstalk issues. The key to achieving high-precision measurements lies in designing a strain FPI sensor insensitive to temperature variations. Therefore, we conducted temperature measurements on FPI. The temperature around the transducer was controlled by a heating table, and the temperature was allowed to stabilize prior to measuring strain response. Figure 9(a) shows the interference spectra of the UATFPI when the temperature was increased from 25°C to 425°C in steps of 100°C, and the temperature was maintained for 20 min at each time. The wavelengths of the reflectance spectra did not change significantly with temperature in this range, proving that the sensor does not experience thermal expansion. As shown in Fig. 9(b), the sensitivity of the UATFPI was 1.56 pm/°C with R^2 values of 0.99586 in the range of 25°C–425°C. The reflectance spectra were insensitive to temperature changes, and a temperature–strain cross talk of 0.0327 με/°C was obtained, indicating a relatively low sensitivity to temperature. Because of the smaller strain error, the sensor requires significantly less temperature compensation during practical detection.

To evaluate the stability of the sensor at different temperatures, we systematically tested the FPI sensor in the temperature range of 25–425°C. Three repeatable stress tests were performed

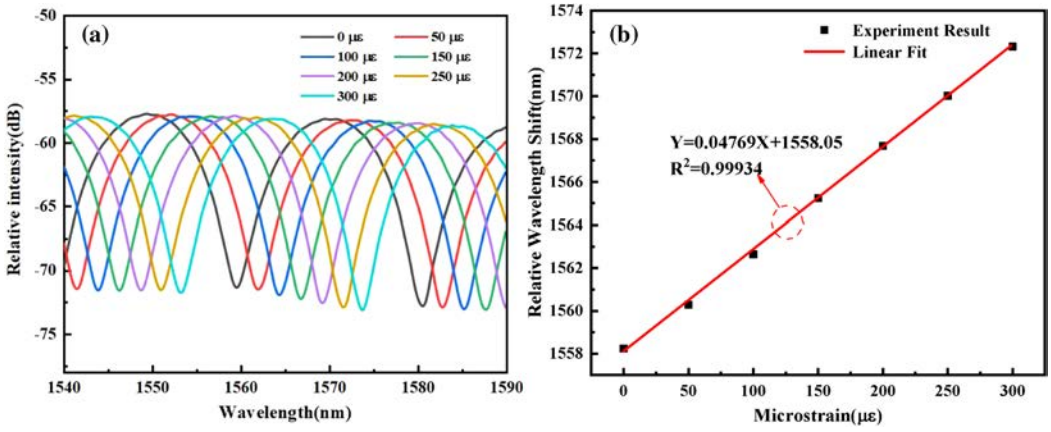

Fig. 7. (a) Reflectance spectra of UATFPI at stresses from 0 to 300 με and (b) linear fit of the UATFPI strain sensitivity.

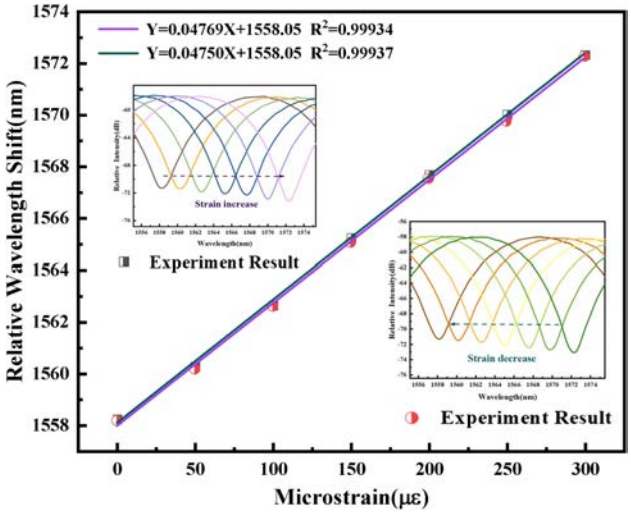

Fig. 8. Repeatability test of the probe.

at each temperature point (25°C, 125°C, 225°C, 325°C, and 425°C) in the forward and reverse stress ranges of 0–300 με. After stabilization at the target temperature, stress was applied in steps of 50 με for 5 min after each stress change and data were recorded. As shown in Figs. 10(a)–10(e), three key performance indicators, namely repeatability, hysteresis effect, and linearity, were adopted to measure the operational stability of the sensor. The sensor functioned stably between 25°C and 425°C with good repeatability, hysteresis, and linearity. In addition, as shown in Fig. 10(f), the strain sensitivity did not change significantly with increasing temperature, indicating that temperature had less effect and the linearity was maintained.

Table 1 compares our sensor with similar strain sensors in the literature in terms of strain range, temperature sensitivity, strain sensitivity, and temperature cross-sensitivity. The conical structure of the microcavity allows a longer propagation path of the light wave through the cavity and increases the interaction with the microcavity compared to the conventional air microcavity, thereby improving the strain sensitivity of the sensor. Besides

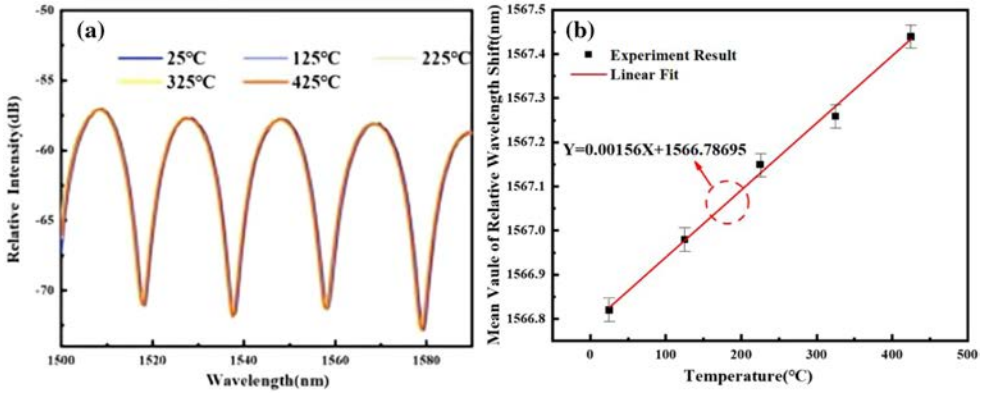

Fig. 9. (a) Reflectance spectra of the UATFPI sensors at different temperatures and (b) relationship between the dip wavelength shift and temperature.

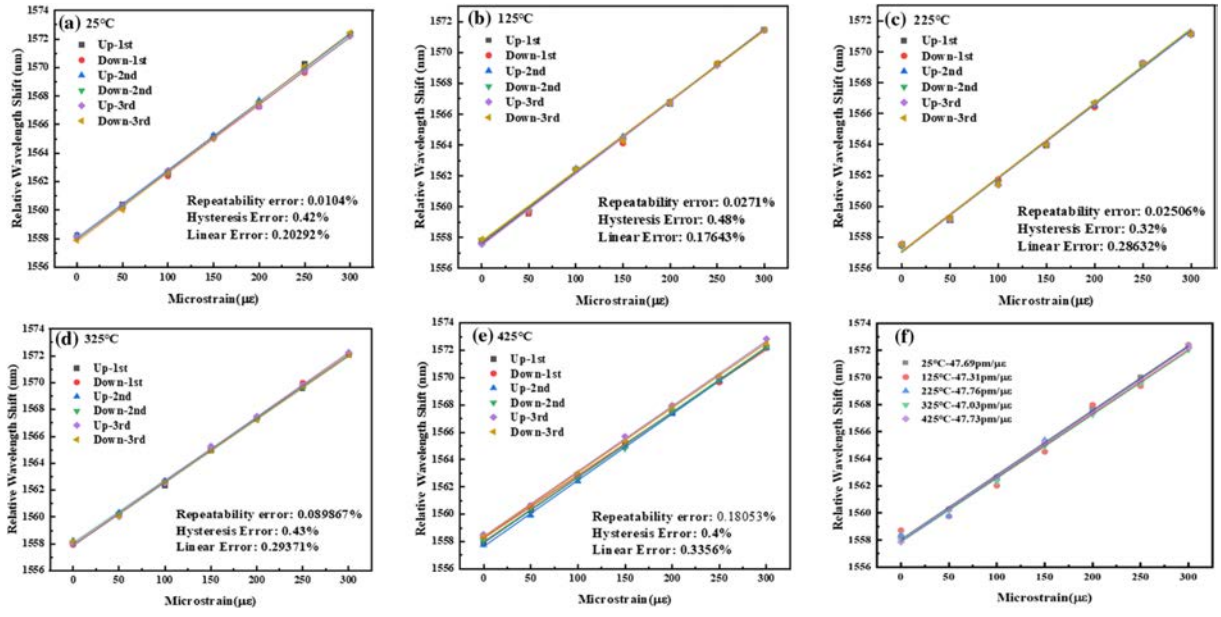

Fig. 10. Results of three stress experiments of UATFPI in the range: (a)–(e) 25°C–425°C in increments of 100°C; (f) strain sensitivity of UATFPI in the range of 25–425°C.

Table 1. Comparison of the Properties of Different Strain Sensors

Reference	Device Structure	Strain Sensitivity (pm/με)	Measurement Range of Strain (με)	Temperature Sensitivity (pm/°C)	Temperature Cross-Sensitivity (με/°C)
[32]	Microsphere embedded	16.2 pm/με	0–150 με	1.4 pm/°C	0.086 με/°C
[35]	Alumina ceramic-derived fiber FPI	1.5 pm/με	0–3000 με	15.6 pm/°C	10.4 με/°C
[36]	Tapered few-mode optical FPI (SMF–FMF–SMF)	−23.9 pm/με	0–450 με	−54.5 pm/°C	2.280 με/°C
[37]	NCF FPI	0.863 pm/με	0–200 με	9.8 pm/°C	11.355 με/°C
[38]	Tapered FBG FPI	1129.44 pm/με	0–200 με	54.58 pm/°C	0.048 με/°C
Our work	Asymmetric tapered	47.69 pm/με	0–300 με	1.56 pm/°C	0.0327 με/°C

having better optical characteristics and versatility, our sensor has resistance to a high temperature and is easier, cheaper, and safer to manufacture.

4. CONCLUSION

A tapered FPI sensor with an asymmetric microcavity that offers high sensitivity and temperature resistance is demonstrated. By means of the arc discharge technique, two single-mode optical fibers are fused together to form a microcavity with an asymmetric tapered structure. The FPI sensor is placed on a heating platform and heated gradually up to 425°C to measure the strain response at 25°C, 125°C, 225°C, 325 °C, and 425°C. The repeatability is confirmed by multiple measurements. The experimental results show that the sensor exhibits a good linear response in the temperature range as well as high strain sensitivity and good temperature stability, confirming that it is operational in high-temperature environments. The strain sensitivity of the sensor is 47.69 pm/με, and the temperature sensitivity is only 1.56 pm/°C. The temperature cross-sensitivity is very small at 0.0327 με/°C. The sensor has large practical potential in strain measurements due to its compact structure, low production cost, good stability, and repeatability.

Funding. National Natural Science Foundation of China (12304480, 62305223); Natural Science Foundation of Heilongjiang Province (JQ2023F001); Local Universities Reformation and Development Personnel Training Supporting Project from Central Authorities, Natural Science Foundation of Heilongjiang Province (LH2021F007); China Postdoctoral Science Foundation (2020M670881); Natural Science Foundation of Guangdong Province (2022A1515110971); Fundamental Project Natural Science Foundation of Heilongjiang Province (LH2022F004); City University of Hong Kong Donation Research Grants (DON-RMG 9229021, 9220061).

Disclosures. The authors declare no conflicts of interest.

Data availability. No data were used for the research described in the paper.

REFERENCES

1. C. Ma, D. Peng, X. Bai, *et al.*, "A review of optical fiber sensing technology based on thin film and Fabry–Perot cavity," Coatings **13**, 1277 (2023).
2. H. Wang, P. Xiang, and L. Jiang, "Strain transfer theory of industrialized optical fiber-based sensors in civil engineering: a review on measurement accuracy, design and calibration," Sens. Actuators A Phys. **285**, 414–426 (2019).
3. X. Liu, J. Miao, Q. Fan, *et al.*, "Recent progress on smart fiber and textile based wearable strain sensors: materials, fabrications and applications," Adv. Fiber Mater. **4**, 361–389 (2022).
4. P. Gu, H. Yang, D. Li, *et al.*, "High-Q and intense lattice plasmon resonance in hexagonal nonclose packed thin silver nanoshells array," J. Phys. Chem. C **128**, 6431–6437 (2024).
5. P. Roriz, L. Carvalho, O. Frazão, *et al.*, "From conventional sensors to fibre optic sensors for strain and force measurements in biomechanics applications: a review," J. Biomech. **47**, 1251–1261 (2014).
6. J. Wang, X. Lu, C. Mi, *et al.*, "Ultra-high sensitivity photonic crystal fiber sensor based on dispersion turning point sensitization of surface plasmonic polariton modes for low RI liquid detection," Opt. Express **32**, 32895–32908 (2024).
7. C. Liu, J. Lü, W. Liu, *et al.*, "Overview of refractive index sensors comprising photonic crystal fibers based on the surface plasmon resonance effect," Chin. Opt. Lett. **19**, 102202 (2021).
8. W. Liu, C. Liu, J. Wang, *et al.*, "Surface plasmon resonance sensor composed of microstructured optical fibers for monitoring of external and internal environments in biological and environmental sensing," Results Phys. **47**, 106365 (2023).
9. X. Rao, H. Zhu, X. Wang, *et al.*, "High-sensitivity plasmonic refractive index sensor based on embedded gratings with triple self-reference characteristics," J. Opt. Soc. Am. B **42**, 431–437 (2025).
10. W. Liu, Y. Shi, Z. Yi, *et al.*, "Surface plasmon resonance chemical sensor composed of a microstructured optical fiber for the detection of an ultra-wide refractive index range and gas-liquid pollutants," Opt. Express **29**, 40734–40747 (2021).
11. T. Chen, J. Gao, X. Wang, *et al.*, "High FOM Fano resonance refractive-index sensor based on a baffled MIM waveguide coupled with an inverted L-shaped resonator," Phys. Scr. **100**, 015533 (2024).
12. S. Ma, Y. Xu, Y. Pang, *et al.*, "Optical fiber sensors for high-temperature monitoring: a review," Sensors **22**, 5722 (2022).
13. Q. Tian, G. Xin, K. S. Lim, *et al.*, "Optical fiber sensor with double tubes for accurate strain and temperature measurement under high temperature up to 1000° C," IEEE Sens. J. **22**, 11710–11716 (2022).
14. J. Han, T. Yang, and X. Wang, "Advanced fiber optic sensing for cryogenic simultaneous temperature and strain measurement," IEEE Trans. Instrum. Meas. **73**, 7005314 (2024).
15. J. Lv, W. Li, J. Wang, *et al.*, "High-sensitivity strain sensor based on an asymmetric tapered air microbubble Fabry-Pérot interferometer with an ultrathin wall," Opt. Express **32**, 19057–19068 (2024).
16. X. Gao, T. Ning, J. Zheng, *et al.*, "Simultaneous measurement of refractive index, strain, and temperature based on a Mach–Zehnder interferometer with hybrid structure optical fiber," Appl. Opt. **58**, 8187–8193 (2019).
17. D. Lu, S. Liao, Y. Chu, *et al.*, "Highly durable and fast response fabric strain sensor for movement monitoring under extreme conditions," Adv. Fiber Mater. **5**, 223–234 (2023).
18. T. Yang, H. Wang, and X. Wang, "Strain transfer characteristics of multi-layer optical fiber sensors with temperature-dependent properties at low temperature," Sensors **21**, 495 (2021).
19. M. Ramakrishnan, G. Rajan, Y. Semenova, *et al.*, "Overview of fiber optic sensor technologies for strain/temperature sensing applications in composite materials," Sensors **16**, 99 (2016).

20. J. Tian, Z. Li, Y. Sun, *et al.*, "High-sensitivity fiber-optic strain sensor based on the Vernier effect and separated Fabry–Perot interferometers," J. Lightwave Technol. **37**, 5609–5618 (2019).
21. H. P. Wang, J. G. Dai, and X. Z. Wang, "Improved temperature compensation of fiber Bragg grating-based sensors applied to structures under different loading conditions," Opt. Fiber Technol. **63**, 102506 (2021).
22. T. Yang and X. Wang, "Decoupling and simultaneous measurement of nonuniform strain and temperature using a single distributed optical fiber ring," Exp. Mech. **62**, 1531–1552 (2022).
23. J. Lv, W. Li, T. Meng, *et al.*, "Low-temperature cross-sensitivity strain sensor based on a microbubble Fabry-Pérot interferometer with a thin wall," Opt. Fiber Technol. **80**, 103452 (2023).
24. J. Wang, W. Liu, Q. Li, *et al.*, "A high-sensitivity strain sensor based on the core-offset fiber with a micro air bubble," Opt. Commun. **555**, 130235 (2024).
25. Z. Lu, C. Liu, C. Li, *et al.*, "Ultra-high sensitivity and temperature-insensitive optical fiber strain sensor based on dual air cavities," Materials **16**, 3165 (2023).
26. Q. Li, J. Wang, H. Mu, *et al.*, "A Fabry–Pérot interferometer strain sensor composed of a rounded rectangular air cavity with a thin wall for high sensitivity and interference contrast," Opt. Commun. **527**, 128920 (2023).
27. G. Zhang, M. Yang, and M. Wang, "Large temperature sensitivity of fiber-optic extrinsic Fabry–Perot interferometer based on polymer-filled glass capillary," Opt. Fiber Technol. **19**, 618–622 (2013).
28. Z. Wang, W. Bao, P. Yang, *et al.*, "Highly sensitive strain sensor based on the Vernier effect with high extinction ratio and low-temperature cross-sensitivity by compact double FPI," IEEE Sens. J. **24**, 7896–7904 (2024).
29. T. Tian, K. Liang, Y. Ma, *et al.*, "A Fabry-Perot interferometer based on probe-embedded bubble for ultrasensitive strain measurement," Measurement **239**, 115505 (2025).
30. C. Su, J. Gao, Y. You, *et al.*, "All-fiber Fabry-Perot micro-cavity temperature-insensitive sensor for strain sensing based on T-shaped structure," Opt. Fiber Technol. **87**, 103880 (2024).
31. S. Chen, Y. Han, J. Li, *et al.*, "Ultra-simple fiber sensor with ultra-low strain cross-sensitivity for embedded temperature detection," Optik **270**, 170028 (2022).
32. K. Tian, M. Zhang, J. Yu, *et al.*, "High sensitivity, low temperature-crosstalk strain sensor based on a microsphere embedded Fabry–Perot interferometer," Sens. Actuators A Phys. **310**, 112048 (2020).
33. Y. J. Rao, M. Deng, D. W. Duan, *et al.*, "Micro Fabry-Perot interferometers in silica fibers machined by femtosecond laser," Opt. Express **15**, 14123–14128 (2007).
34. A. R. Bunsell, "Oxide fibers for high-temperature reinforcement and insulation," JOM **57**, 48–51 (2005).
35. Z. Wang, H. Liu, Z. Ma, *et al.*, "High temperature strain sensing with alumina ceramic derived fiber based Fabry-Perot interferometer," Opt. Express **27**, 27691–27701 (2019).
36. L. Li, C. Jiang, C. Hu, *et al.*, "Highly sensitive strain sensor based on tapered few-mode fiber," Rev. Sci. Instrum. **94**, 075006 (2023).
37. C. Zhu, O. Alsalman, and J. Huang, "Fs-laser fabricated miniature Fabry–Perot interferometer in a no-core fiber for high-temperature applications," Sensors **23**, 7754 (2023).
38. X. Zhao, Y. Zhang, W. Zhang, *et al.*, "Ultra-high sensitivity and temperature-compensated Fabry–Perot strain sensor based on tapered FBG," Opt. Laser Technol. **124**, 105997 (2020).